Naval Research Laboratory
Washington, DC 20375-5320

NRL/5610/MR—2023/1

Coherent and Incoherent Light Separation Using Image Plane Vortex Phase Masks

ABBIE T. WATNIK
SHAWN DIVITT
MATTHEW HART

Aerosol Optics Section
Optical Sciences Division

February 27, 2023

REPORT DOCUMENTATION PAGE

Form Approved
OMB No. 0704-0188

1. REPORT DATE *(DD-MM-YYYY)*	**2. REPORT TYPE**	**3. DATES COVERED** *(From - To)*
27-02-2023	NRL Memorandum Report	06-30-2022 – 12/20/2022

4. TITLE AND SUBTITLE

Coherent and Incoherent Light Separation Using Image Plane Vortex Phase Masks

5a. CONTRACT NUMBER

5b. GRANT NUMBER

5c. PROGRAM ELEMENT NUMBER

6. AUTHOR(S)

Abbie T. Watnik, Shawn Divitt, and Matthew Hart

5d. PROJECT NUMBER

5e. TASK NUMBER

5f. WORK UNIT NUMBER
6C42

7. PERFORMING ORGANIZATION NAME(S) AND ADDRESS(ES)

Naval Research Laboratory
4555 Overlook Avenue, SW
Washington, DC 20375-5320

8. PERFORMING ORGANIZATION REPORT NUMBER

NRL/5610/MR--2023/1

9. SPONSORING / MONITORING AGENCY NAME(S) AND ADDRESS(ES)

Naval Research Laboratory
4555 Overlook Avenue, SW
Washington, DC 20375-5320

10. SPONSOR / MONITOR'S ACRONYM(S)
NRL

11. SPONSOR / MONITOR'S REPORT NUMBER(S)

12. DISTRIBUTION / AVAILABILITY STATEMENT

DISTRIBUTION STATEMENT A: Approved for public release; distribution is unlimited.

13. SUPPLEMENTARY NOTES

14. ABSTRACT

We consider the application of a modified optical vortex coronagraph as a transmissometer. We find, through theory and simulation, that the rejection of scattered light benefits from increasing the charge number of the vortex masks in the image plane, and that a combination of vortex mask and binary pinhole can outperform the pinhole alone.

15. SUBJECT TERMS

Transmissometry
Vortex
Scattering mitigation
Coronagraph

16. SECURITY CLASSIFICATION OF:			**17. LIMITATION OF ABSTRACT**	**18. NUMBER OF PAGES**	**19a. NAME OF RESPONSIBLE PERSON**
					Shawn Divitt
a. REPORT	**b. ABSTRACT**	**c. THIS PAGE**	U	16	**19b. TELEPHONE NUMBER** *(include area code)*
U	U	U			(202) 767-5381

This page intentionally left blank.

Coherent and Incoherent Light Separation Using Image Plane Vortex Phase Masks

ABBIE T. WATNIK,[1,*] SHAWN DIVITT,[1] AND MATTHEW HART[1]

[1] *U.S. Naval Research Laboratory, Washington, DC 20375*
[*] *abbie.watnik@nrl.navy.mil*

Abstract: We consider the application of a modified optical vortex coronagraph as a transmissometer. We find, through theory and simulation, that the rejection of scattered light benefits from increasing the charge number of the vortex masks in the image plane, and that a combination of vortex mask and binary pinhole can outperform the pinhole alone.

1. Introduction

The optical vortex coronagraph, so-called because it employs an optical vortex phase element, was originally developed in astronomy to distinguish an exoplanet from a star [1–3]. Theoretically, neglecting scattering and optical aberration, this type of coronagraph can completely remove the relatively much brighter background starlight from the image of an exoplanet, allowing it to be seen [4]. More recently, the ability of a vortex phase element to distinguish spatially coherent from spatially incoherent sources has been leveraged for use in transmissometers [5, 6], revealing an opportunity for the optical vortex coronagraph to be used in a transmissometer mode.

Variations on using a phase element/mask as a scattering discrimination device have been previously tested in several configurations. Palacios et al. [1] describe placing an $m = 1$ vortex mask, where m is the topological charge or number of 2π phase wraps, in front of a lens and array detector. A schematic is given in Fig. 1(a). The geometry allowed for nulling of unscattered coherent light such that only scattered light was present at the optical axis.

Cochenour et al. [5] placed an $m = 8$ vortex phase mask in front of an array detector, without a lens, to generate a ring of coherent light such that only scattered light was present in a core region about the optical axis. A schematic is given in Fig. 1(b). This allowed for measurement of the ratio between coherent and incoherent light power on the detector. They demonstrated measurements of the ratio that followed Beer's law at attenuation lengths of up to around 4.5. Jantzi et al. [7, 8] employed an axicon instead of a vortex mask to produce coherent-incoherent power ratio plots similar to those of Cochenour and were able to measure a curve that closely followed Beer's law to around 14 attenuation lengths before levelling off.

The systems described above were successful in separating coherent, unscattered light from incoherent, scattered light at modest attenuation lengths. However, they suffer from a fairly large field of view, accepting a large amount of scattered light relative to unscattered light. Ultimately, shot noise from the scattered signal overwhelmed the coherent signal in each case. We expect a system in the spirit of Palacios, Cochenour, and Jantzi, but with a much smaller field of view, to greatly outperform these earlier systems. Specifically, we are interested in using a modified optical vortex coronagraph to reject scattered light while relaying unscattered light to the detector.

2. The Optical Vortex Coronagraph

2.1. Theory

Although the theoretical underpinnings of the optical vortex coronagraph have been developed and described elsewhere (e.g. Swartzlander [3]) it is important that we summarize the key points here, as we will draw upon that foundation in this work.

Manuscript approved February 24, 2023.

First, it is known that the Fourier transform of a circular aperture of radius R can be described as a zeroth-order Hankel transform, producing an Airy disk. When this term is multiplied by a vortex of even-numbered charge m, namely, $e^{im\phi}$, the field distribution of its inverse Fourier transform becomes (cf. [3], Eq. 4)

$$E(r,\theta) = i^m e^{im\theta} R H_m \left\{ J_1(k_\rho R)/(k_\rho R) \right\}_{\rho \to r} \tag{1}$$

where $H_m \{g(\rho)\}_{\rho \to r}$ is the mth order Hankel transform of the test function $g(\rho)$ from ρ to r, $J_1(x)$ is the Bessel J function, $k_\rho := 2\pi\rho/(\lambda f)$, λ is the wavelength, f is the focal length of the transform lens, r is the radial coordinate and θ is the angular coordinate. Swartzlander shows that this function features an extended central region over which the value is identically zero. This means that a point source, imaged onto the singularity at the center of a vortex plate of even-numbered charge after passing through an entrance pupil of finite radius, will produce a completely dark region σ surrounded by a "ring of fire" in the Fourier plane, while a point source that is not centered on the phase singularity will produce a pattern that features light within σ. Under perfect, infinitely large lenses, a Lyot stop placed in the relevant plane will block all of the light originating from the on-axis source and pass only light from off-axis sources. This system is interesting in astronomy applications where one wants to reject light from a bright source in order to detect light from a dimmer, nearby source.

2.2. Optical Configuration

Our goal in this case it to find a system that accepts light from only a single point in 3D space while rejecting light emitted from any other position. An interesting candidate system to accomplish this goal is the vortex coronagraph in a new modality where the Lyot stop is replaced with a central obscuration. Such a system would pass light from an on-axis, in-focus point source while greatly attenuating off-axis and out-of-focus sources.

Swartzlander [3] limited the discussion to even-number charged vortex plates because odd-number charged plates do not produce a perfect-null central region. Here, we are not similarly limited because we wish to maximize the on-axis passed power relative to the off-axis power that leaks around the central obscuration and do not expect any completely dark regions given finite-sized lenses. A schematic for an optical vortex coronagraph is shown in Fig. 1 (c). Incoming coherent light is focused by L_1 on-axis in the plane of a vortex phase mask. The lens L_2 provides an optical Fourier transform of the field just after the vortex mask at the position of the Lyot stop. The Lyot stop is the component that directly blocks the on-axis light, after being transformed into a "ring of fire" by the vortex mask, but allows off-axis light to pass.

As we envision separation of coherent and incoherent light for the application of a scatterometer, we consider replacing the binary Lyot stop with an object of the opposite polarity: a central beam block. Figure 1(d) shows the configuration where coherent light that creates a "ring of fire" is transmitted, but where off-axis, incoherent light is absorbed by a beam block. The coherent light can then be focused by the lens $L3$ onto an array or bucket detector to measure the total coherent power through the device.

The distinction between the scatterometer geometry in this work and the previous work by Palacios et al [1] and Jantzi et al [9] is the insertion of the vortex phase mask in an intermediate image plane of the imaging system, not adjacent to an imaging lens, as done in these previous works. The unique property of the vortex phase mask in the imaging plane, as described by the optical vortex coronagraph design, is the resultant coherent "ring of fire." Unlike the previous geometries which resulted in spatial overlap of incoherent light in the coherent region, this geometry ideally spatially separates coherent from incoherent light. This unique property should not be understated; unlike previous work that had to utilize temporal gating to reduce the scattered light [9], this approach does not rely on additional scatter suppression mechanisms. The realization of an optical vortex coronagraph scatterometer was first described by Wan et

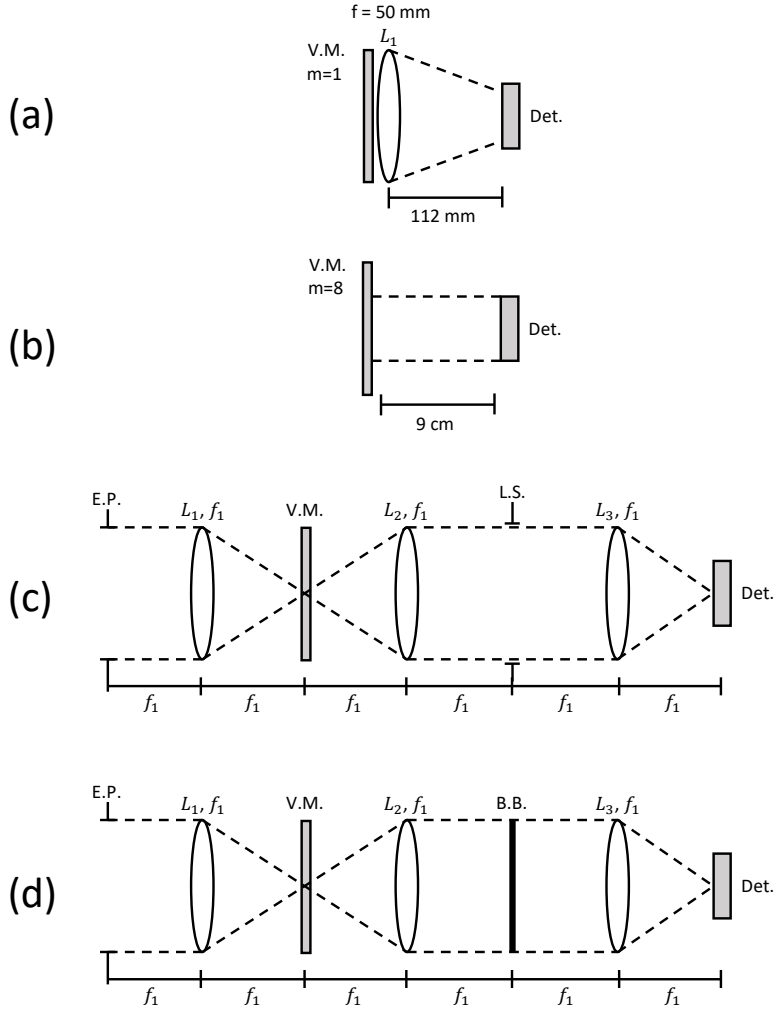

Fig. 1. Optical configurations for (a) Palacios et al. [1], (b) Cochenour et al. [5], (c) an optical vortex coronagraph (c.f. [3]), (d) this work. V.M. indicates a vortex mask, E.P. indicates an entrance pupil, L.S. indicates a Lyot stop, B.B. indicates a beam block, and Det. indicates a detector.

al [2]. The Wan paper describes an experimental demonstration of the technique with a vortex phase plate of $m = 2$.

3. Coherence Properties of Scattering Media

Here, we introduce some important results from optical coherence theory before applying them in simulation. We are specifically interested in the coherence of the light field at a plane beyond the scattering medium, for example at the entrance pupil of an optical system. As spatially coherent light propagates through a scattering medium, such as a laser beam through turbid water, the coherence of the light field can be changed due to scattering. This change in coherence can be exploited to filter scattered light from unscattered light. In general, we can describe the total

light field $U(\mathbf{r}, \omega)$ as the sum of the incident field $U^{(\mathrm{i})}(\mathbf{r}, \omega)$ and the scattered field $U^{(\mathrm{s})}(\mathbf{r}, \omega)$:

$$U(\mathbf{r}, \omega) = U^{(\mathrm{i})}(\mathbf{r}, \omega) + U^{(\mathrm{s})}(\mathbf{r}, \omega) \tag{2}$$

where $\mathbf{r}$ is the spatial position vector and ω is the field frequency (cf. [10], Eq. 6.1.9). The cross-spectral density, which is the covariance between two fields of frequency ω at positions $\mathbf{r}_1$ and $\mathbf{r}_2$, is given by (cf. [10], Eq. 4.1.13)

$$\begin{aligned} W(\mathbf{r}_1, \mathbf{r}_2, \omega) &:= \langle U^*(\mathbf{r}_1, \omega)\, U(\mathbf{r}_2, \omega)\rangle_\omega \qquad (3)\\ &= \left\langle U^{(\mathrm{i})*}(\mathbf{r}_1, \omega)\, U^{(\mathrm{i})}(\mathbf{r}_2, \omega)\right\rangle_\omega + \left\langle U^{(\mathrm{s})*}(\mathbf{r}_1, \omega)\, U^{(\mathrm{s})}(\mathbf{r}_2, \omega)\right\rangle_\omega \\ &\quad + 2\mathrm{Re}\left\{\left\langle U^{(\mathrm{i})*}(\mathbf{r}_1, \omega)\, U^{(\mathrm{s})}(\mathbf{r}_2, \omega)\right\rangle_\omega\right\} \qquad (4) \end{aligned}$$

where $*$ represents the complex conjugate and $\langle f(\omega)\rangle_\omega$ is the ensemble average of the test function f over quasi-monochromatic realizations of the field at frequency ω. If the incident and scattered fields are completely uncorrelated over the entire pupil then the cross-term drops out and Eq. 4 can be rewritten simply as

$$W(\mathbf{r}_1, \mathbf{r}_2, \omega) = W^{(\mathrm{i})}(\mathbf{r}_1, \mathbf{r}_2, \omega) + W^{(\mathrm{s})}(\mathbf{r}_1, \mathbf{r}_2, \omega) \tag{5}$$

where $W^{(\mathrm{i})}$ and $W^{(\mathrm{s})}$ and the cross-spectral densities of the incident and scattered fields alone. Essentially, this means that we can model the intensity of light in the entrance pupil as the sum of the incident and scattered field intensity contributions, assuming that they are uncorrelated.

At this point it is useful to introduce the spatial degree of coherence μ, which is the correlation coefficient between fields at two points in space (cf. [10], Eq. 4.2.6a):

$$\mu(\mathbf{r}_1, \mathbf{r}_2, \omega) := \frac{W(\mathbf{r}_1, \mathbf{r}_2, \omega)}{\sqrt{W(\mathbf{r}_1, \mathbf{r}_1, \omega)}\sqrt{W(\mathbf{r}_2, \mathbf{r}_2, \omega)}}. \tag{6}$$

The value of μ is generally complex and bounded in magnitude between 0 and 1 (cf. [10], Eq. 4.2.9), where a magnitude of 1 would indicate perfect correlation and a magnitude of 0 would indicate no correlation. With a coherent source, such as a laser or a point source, unscattered light will maintain its spatial coherence at the entrance pupil. That is, $\left|\mu^{(\mathrm{i})}(\mathbf{r}_1, \mathbf{r}_2)\right| \approx 1$ for all $\mathbf{r}_1$ and $\mathbf{r}_2$ in the pupil. In contrast, upon elastic scattering in turbid water, photons can change their direction randomly, resulting in random phase variations and partially coherent light at the entrance pupil. The magnitude of $\mu^{(\mathrm{s})}$ will depend, in general, on the number of times the light has scattered (the distribution of path length). The greater the number of scattering events, the lower the degree of coherence at the pupil. Random changes in the scattering medium during the exposure time of a detector will also lead to a decrease in the measured degree of spatial coherence.

For example, with strongly scattering turbid water as the propagation medium between the source and the optical system, we expect the scattered field at the entrance pupil to act as though it was emitted by a spatially incoherent source. It is important to note that such a source does not imply $\left|\mu^{(\mathrm{s})}(\mathbf{r}_1, \mathbf{r}_2)\right| \approx 0$ at all $\mathbf{r}_1$ and $\mathbf{r}_2$ in the pupil where $\mathbf{r}_1 \neq \mathbf{r}_2$. It is well known that incoherent sources can create partially coherent fields at a distance (see [10], Sec. 3.2). Rather, treating the turbid water as an incoherent source allows us to simulate the intensity at the image plane of the optical system by propagating an ensemble of uncorrelated plane waves from the entrance aperture through the system to the image plane and adding up the intensities, which is essentially the same idea used in deriving the van Cittert-Zernike theorem.

Based on the above analysis, we can filter the scattered light from the unscattered light by using an optical system that generates starkly different images depending on whether the source is a single point or an extended, spatially incoherent source. The optical vortex mask allows us to create one such system.

4. The Optical Vortex as a Coherence Filter

When considering the use of the optical vortex coronagraph as a coherence filter in a scattering regime, the property that is being exploited is directly related to the phase properties of unscattered versus scattered light. The optical vortex coronagraph scatterometer takes advantage of the fact that unscattered, spatially coherent light can be shaped by a vortex phase mask while the scattered light will not. Under ideal conditions, with infinitely large, diffraction-limited lenses, the separation between the incoherent and coherent light approaches perfection: all coherent light is transformed outside the aperture to a "ring of fire" and all but a tiny fraction of the incoherent light is relayed inside the image of the aperture; the tiny faction is due to diffraction by the vortex mask. Essentially, there is a sharp transition and cutoff exactly at the edge of entrance pupil image. Practically, however, it is impossible to actualize this sharp transition. Experimental defects, finite sized optics, non-ideal wavefronts, misalignment, dust, non-circular apertures and other imperfections can all contribute to coherent intensity components within the ring of fire [3], as well as incoherent intensity components outside of the ring.

Here, we examine the coherent-to-incoherent power ratio on the detector as a function of vortex charge, m, and beam block radius R_b. Ideally, a beam block radius equal to the radius R_0 of the entrance pupil would block all incoherent light and the ratio would approach infinity. In a real system, with finite beam sizes and optics, the ratio will be finite although it will still undergo a large change near $R_b = R_0$. We quantify the coherent-incoherent (CI) ratio to determine the most appropriate beam block size which allows for the highest CI ratio. Our results show that the radius of the beam block, i.e. highest CI ratio, is dependent on optical vortex charge number.

We model the optical system diagrammed in Fig. 1(d) numerically, using standard Fourier optical methods of wave propagation (see [11], Chaps. 5 and 6). We are interested primarily in the intensity at the plane of the beam block, which is the rear focal point of lens L_2. At that plane we can determine the optimal beam block radius by examining the intensity patterns created by the coherent and incoherent (scattered) inputs. Under the Fresnel (paraxial) and scalar field approximations, the field U_v just before the vortex mask is given by the Fourier transform of the field in the entrance pupil (c.f. [11], Eq. 5-19):

$$U_v(x,y) \propto \iint_{-\infty}^{\infty} t_A(\xi,\eta) \exp\left(-\mathrm{i}\frac{2\pi}{\lambda f_1}\left[x\xi + y\eta\right]\right) \mathrm{d}\xi \mathrm{d}\eta, \tag{7}$$

where t_A is the field at the entrance pupil, f_1 is the lens focal length, and λ is the light wavelength. Given a circular entrance pupil of radius R_0 and a plane wave arriving from the direction defined by polar angle θ and azimuthal angle ϕ, we have

$$t_A(x,y) = \exp\left(\mathrm{i}2\pi\left[\frac{\sin\theta\cos\phi}{\lambda}x + \frac{\sin\theta\sin\phi}{\lambda}y\right]\right) \mathrm{circ}\left(\frac{\sqrt{x^2+y^2}}{R_0}\right). \tag{8}$$

The field at the beam block plane, U_b, is given by the Fourier transform of the product of U_v with the vortex phase plate of topological charge m,

$$U_b(x,y) \propto \iint_{-\infty}^{\infty} U_v(\xi,\eta) \exp\left(\mathrm{i}\, m\, \mathrm{atan2}\left[\eta,\xi\right]\right) \exp\left(-\mathrm{i}\frac{2\pi}{\lambda f_1}\left[x\xi + y\eta\right]\right) \mathrm{d}\xi \mathrm{d}\eta, \tag{9}$$

where atan2 is the two-argument arctangent. The spatial function $|U_b(x,y)|^2$ gives the intensity of the light at the beam block plane as predicted by geometrical optics, that is, without accounting for diffraction due to lenses.

To account for the finite extent of real lenses, we assume that our optics are diffraction-limited with a spatially invariant amplitude impulse response $h(x,y)$. As described by Goodman [11], pg. 131, "we can regard the image as being a convolution of the image predicted by geometrical

optics with an impulse response that is the Fraunhofer diffraction pattern of the exit pupil." Here, since we are interested in the intensity at the beam block plane, which is the image plane of the entrance pupil, we can regard the entrance pupil itself as the object being imaged, which makes lens L_1 the aperture stop of the two-lens imaging system. This implies that the exit pupil is a circle of radius R_L equal to that of L_1 at a position $2f_1$ beyond L_2. Specifically (c.f. [11], Eq. 6-5)

$$h(x,y) \propto \iint_{-\infty}^{\infty} \operatorname{circ}\left(\frac{\sqrt{\xi^2+\eta^2}}{R_L}\right) \exp\left(-\mathrm{i}\frac{2\pi}{\lambda z_i}(x\xi+y\eta)\right) \mathrm{d}\xi\mathrm{d}\eta \tag{10}$$

$$\propto \operatorname{jinc}\left(\frac{2\pi R_L}{\lambda f_1}\sqrt{x^2+y^2}\right) \tag{11}$$

where $z_i = f_1$ is the distance between the image plane and the exit pupil, $\operatorname{jinc}(x) := J_1(x)/x$, and $J_1(x)$ is the Bessel J function.

The amplitude impulse response function h is used to determine the expected intensity distribution $I(x,y)$ under the influence of diffraction, but it is used differently depending on the field coherence. In the coherent case we have (c.f. [11], Eq. 6-12)

$$I_c(x,y) \propto \left| \iint_{-\infty}^{\infty} h(x-\xi, y-\eta) U_b(\xi,\eta) \mathrm{d}\xi\mathrm{d}\eta \right|^2, \tag{12}$$

where we use a single value for the polar angle $\theta = 0$ inside of t_A. In the incoherent (scattered) case we have (c.f. [11], Eq. 6-15)

$$I_i(x,y) \propto \iint_{-\infty}^{\infty} |h(x-\xi, y-\eta)|^2 \, I_b(\xi,\eta) \mathrm{d}\xi\mathrm{d}\eta \tag{13}$$

where $I_b = \left\langle U_b^* U_b \right\rangle$ is the ensemble average over the intensities of quasi-monochromatic realizations of the random field U_b given a density of angles θ in t_A. These convolutions can be quickly calculated by applying the convolution theorem of Fourier transforms. Let $\mathcal{F}\{g(x,y)\}(f_x,f_y)$ indicate the ordinary, unitary Fourier transform of the test function g from coordinates x,y to f_x, f_y and let $\mathcal{F}^{-1}\left\{G(f_x,f_y)\right\}(x,y)$ indicate the inverse Fourier transform. Then

$$I_c(x,y) \propto \left|\mathcal{F}^{-1}\left\{\mathcal{F}\{h\}\mathcal{F}\{U_b\}\right\}\right|^2, \text{ and} \tag{14}$$

$$I_i(x,y) \propto \mathcal{F}^{-1}\left\{\mathcal{F}\left\{|h|^2\right\}\mathcal{F}\{I_b\}\right\}. \tag{15}$$

The function $\mathcal{F}\{h\}$ is known as the amplitude transfer function, while the function $\mathcal{F}\left\{|h|^2\right\}$ is known as the optical transfer function or OTF. Here, we have

$$\mathcal{F}\{h(x,y)\}(f_x,f_y) = \operatorname{circ}\left(\frac{\lambda f_1}{R_L}\sqrt{f_x^2+f_y^2}\right), \tag{16}$$

and (c.f. [11], Eq. 6-32)

$$\mathcal{F}\left\{|h(x,y)|^2\right\}(f_x,f_y) = \begin{cases} \frac{2}{\pi}\left(\arccos\left[\frac{\rho}{2\rho_0}\right] - \frac{\rho}{2\rho_0}\sqrt{1-\left(\frac{\rho}{2\rho_0}\right)^2}\right) & \rho \le 2\rho_0 \\ 0 & \text{otherwise} \end{cases} \tag{17}$$

where $\rho := \sqrt{f_x^2+f_y^2}$ and $\rho_0 := R_L/(\lambda f_1)$.

5. Numerical Simulation: Parameters

To find the distributions of I_c and I_i it remains to find the distributions of U_b and I_b. We do this numerically for a specific case with parameters that are reasonable for a laboratory experiment. Using Eq. 9, we simulate an ensemble of infinite plane waves with wavelength 532 nm that strike the entrance pupil aperture of radius $R_0 = 0.5$ mm. Lenses L_1 and L_2 are identical and diffraction-limited, with diameter 25.4 mm and focal length 150 mm. To model the coherent and incoherent complex optical field components, we take into account the incoming incident angle of the wave. The system is oriented so that the coherent light contribution is determined by the single plane wave that arrives exactly on-axis, with a flat wavefront in the entrance pupil, and aligned with the singularity at the center of the vortex phase mask in the intermediate image plane. To synthesize the incoherent contributions, we propagate a set of plane waves at polar angles θ between 0 to 4 degrees and azimuthal angles ϕ in the full range between 0 and 360 degrees, implying a system full field of view of 8 degrees. This field of view was chosen to avoid the complication of vignetting by the lenses, although we do not expect a larger field of view to greatly affect the conclusions. The incoherent intensity in the pupil plane will be the sum of the intensities of the individual plane wave components, as described by the van Cittert-Zernike theorem. Essentially, the incoherent turbid-medium source is treated as a distant, spatially incoherent, spherical cap source with an 8 degree angular subtense where the center of the cap is located on the optical axis.

The domain of polar angles must be sampled carefully to extract the correct image of the incoherent source from the simulated optical system. The focus of L_1 overlaps the singularity of the vortex plate for only very small angles θ, but because the behavior of the system is starkly different for those angles than for larger θ, a significant fraction of the power found outside of radius R_0 in the back focal plane of L_2 (the beam block plane) is due to the waves originating from those small angles. The image of the entrance pupil in the vortex mask plane will be an Airy disk, which is the squared modulus of the jinc/besinc/sombrero function. The first null of the disk will overlap the vortex singularity for $\theta \approx \theta_j := 3.83\lambda/(2\pi R_0)$ radians ≈ 0.0372 degrees. We sample 100 equally spaced angles θ between 0 and $2\theta_j$, which finely samples the main two lobes of the disk and the majority of the power as it overlaps the singularity. We sample 100 more, equally spaced angles θ between $2\theta_j$ and 4 degrees, where the disk and singularity do not significantly overlap. The probability density of a plane wave arriving from a given polar angle θ is directly proportional to $\sin\theta$, while ϕ is described by a uniform probability density function. To account for this, we propagate the waves of each of the 200 angles θ through the optical system at $\phi = 0$ and sum them in intensity, each weighted by $\sin\theta$ and the variable sampling width $\Delta\theta$. The resulting intensity image is used to create a further ensemble in ϕ by rotating the image about the optical axis 150 times, in equal increments, and then summing over the ensemble.

The simulated intensity images span a dynamic range of up to 10 decades, raising concerns with convergence and aliasing in important, low-intensity regions. To ensure that the results converged, the simulations were performed repeatedly using grid resolutions of $2^{13} \times 2^{13}$, $2^{14} \times 2^{14}$, and $2^{15} \times 2^{15}$. The real-space dimensions encompassed a square region of 38.1×38.1 mm (1.5×1.5 inches), which is large enough to avoid any significant aliasing. The difference in results between the 2^{14} and 2^{15} resolutions was minimal, indicating successful convergence and real optical phenomena.

6. Numerical Simulation: Results and Discussion

6.1. Vortex mask and beam block

Figure 2 shows the 2D spatial distribution of the incoherent (left) and coherent (right) intensity, respectively, created by the optical setup given in Fig. 1(d) using a vortex mask with charge $m = 2$. These idealized images include diffraction due to the vortex phase mask but assume

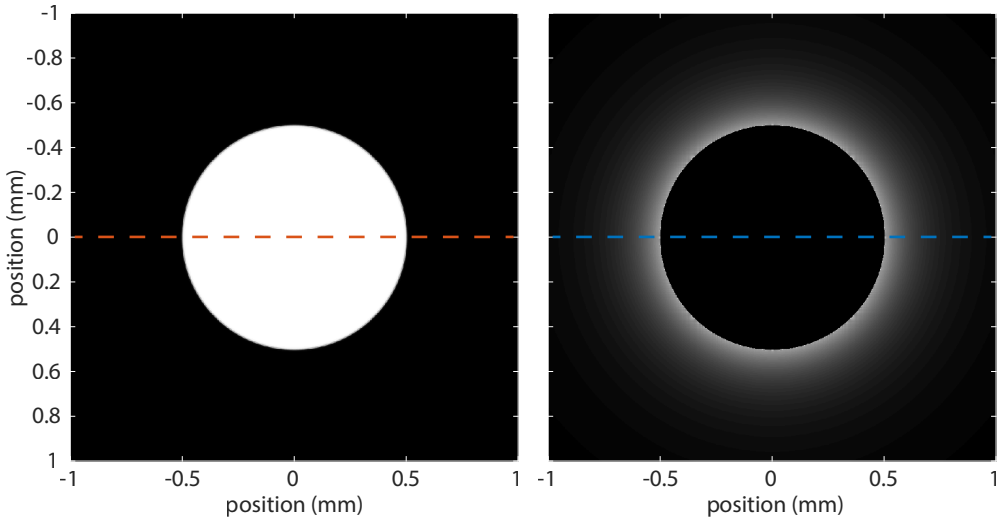

Fig. 2. Distribution of intensity due to incoherent (left) and coherent (right) sources at the pupil (beam block) plane of the imaging system of Fig. 1(d), with a vortex phase mask of charge $m = 2$, in the absence of diffraction due to optics other than the vortex mask itself. The dotted lines indicate the positions of the cross-sections shown in Fig. 3.

infinitely large lenses, as described by Eq. 9. The coherent light forms a "ring of fire" outside the pupil aperture while the incoherent light uniformly fills the aperture. Normalized cross sections of these distributions, indicated by the dotted lines in Fig. 2, are given in Fig. 3. The image created under coherent illumination is greatly different and almost inverse to that created under incoherent illumination. The inversion is not perfect and some power arrives outside of the circle defined by the entrance aperture, due to the weak interaction between the incoherent light and the vortex mask. Blurring due to finite-sized optics would further spread the light outside the circle.

We are interested in determining the optimal beam block size while including the effects of finite optics. To find this size, we define a value that represents the fraction of power in the beam block plane that escapes around a perfectly absorbing circular beam block of radius r. Let $P_x(r) := \int_r^\infty r' I_x(r') \mathrm{d}r'$ be the integrated power outside of the beam block, which is possible to describe using a 1-dimensional integral because the intensity patterns are radially symmetric, and where x can be either c or i indicating the coherent or incoherent intensity patterns. The fraction of power that escapes a beam block of radius r is given by $F_x(r) := P_x(r)/P_0$, where P_0 is the total input power. The CI ratio (the direct ratio of escaping powers between coherent and incoherent patterns) is given by $Q_A(r) := F_c(r)/F_i(r)$. The value of r that maximizes $Q_A(r)$ represents the radius of the beam block that would maximize the signal-to-background-noise ratio in an experiment that uses the optical configuration shown in Fig. 1 (d). However, signal-to-background-noise is not the only quantity of concern in an experiment. The best experimental case is when the output of the detector is signal-shot-noise limited, which depends purely on the signal power. For that reason we introduce an alternative ratio given by $Q_B(r) := F_c^2(r)/F_i(r) = Q_A(r)F_c(r)$, which weights the CI ratio by the coherent power fraction to account for signal power.

Plots of the power ratio functions are given in Fig. 4, after including the effects of finite optics using Eqs. 14 and 15. The escaping coherent power fraction, $P_c(r)$, is shown in Fig. 4(a). The plot shows that higher vortex charge numbers will spread light further beyond the entrance aperture radius R_0 without sacrificing a lot of power. For example, around 80% of the power lies beyond $r = 3R_0$ for the $m = 9$ mask. The escaping incoherent power fraction, $P_i(r)$, is shown in Fig. 4(b). This plot shows that increasing vortex charge only weakly affects the escaping

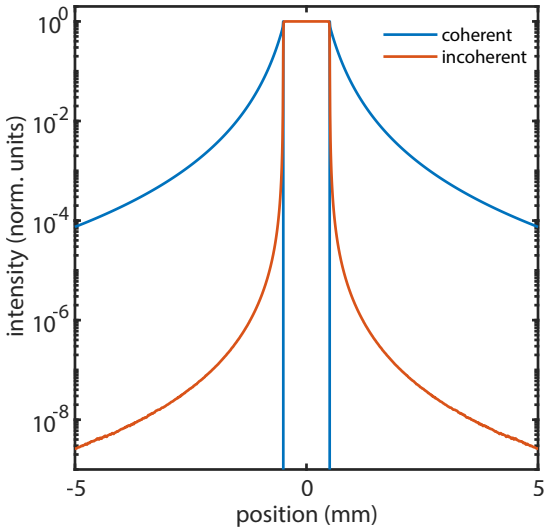

Fig. 3. Normalized cross-sections of the intensity distributions of coherent and incoherent images with a vortex phase mask of $m = 2$ across the dotted lines indicated in Fig. 2 with the corresponding colors.

incoherent power fraction. The escaping power CI ratios $Q_A(r)$ and $Q_B(r)$ are shown in Figs. 4(c) and 4(d), respectively. Here, we find that the ratio maxima increase in magnitude and move towards higher r with increasing vortex charge m. The r position of the maxima of both Q_A and Q_B (arg max Q_A and arg max Q_B) appear to increase close to linearly with charge. Given a particular m, arg max Q_A is always larger than arg max Q_B. A summary of the filtering ability of various vortex masks is presented in Table 1. The vortex mask with charge $m = 9$ outperforms those with charges 2 through 8, and it seems likely that the trend of larger maximum CI ratios under higher charge numbers continues beyond $m = 9$.

6.2. *Pinhole spatial filter*

The optical configuration of Fig. 1(d) can be thought of as an imaging system with an extremely narrow field of view, the purpose of which is to reject any light that is not arriving exactly on-axis. Another optical system that accomplishes this goal is shown in Fig. 5(a). Here, the vortex phase mask is replaced with a pinhole and the beam block is removed. Essentially, a distant source is imaged onto the pinhole and any off-axis parts of the image are blocked. The field just before the pinhole is described by Eq. 7. Here, L_1 is both the entrance and exit pupil with an amplitude impulse response given by Eq. 11. The expected intensity patterns at the pinhole plane are given by Eqs. 14 and 15, except U_b must be replaced with U_v. Similarly, we can define a ratio of escaping power to determine the efficacy of the pinhole at rejecting incoherent power relative to coherent power. Let $p_x(r) := \int_0^r r' I_x(r') \mathrm{d}r'$ be the power that would be passed by a pinhole of radius r, where again the x can be either c or i indicating coherent or incoherent power. The fraction of total incident power that escapes the pinhole is given by $f_x(r) := p_x(r)/P_0$, where P_0 is the total input power. The direct ratio of escaping powers between coherent and incoherent sources is given by $Q_A(r) := f_c(r)/f_i(r)$, and the coherent-power-weighted CI ratio of escaping powers is given by $Q_B(r) := f_c^2(r)/f_i(r) = Q_A(r) f_c(r)$.

Plots of the CI ratio functions for the pinhole setup are given in Figs. 6(a) and 6(b). A Dirac delta impulse response function was used in generating the blue curves, thus eliminating light

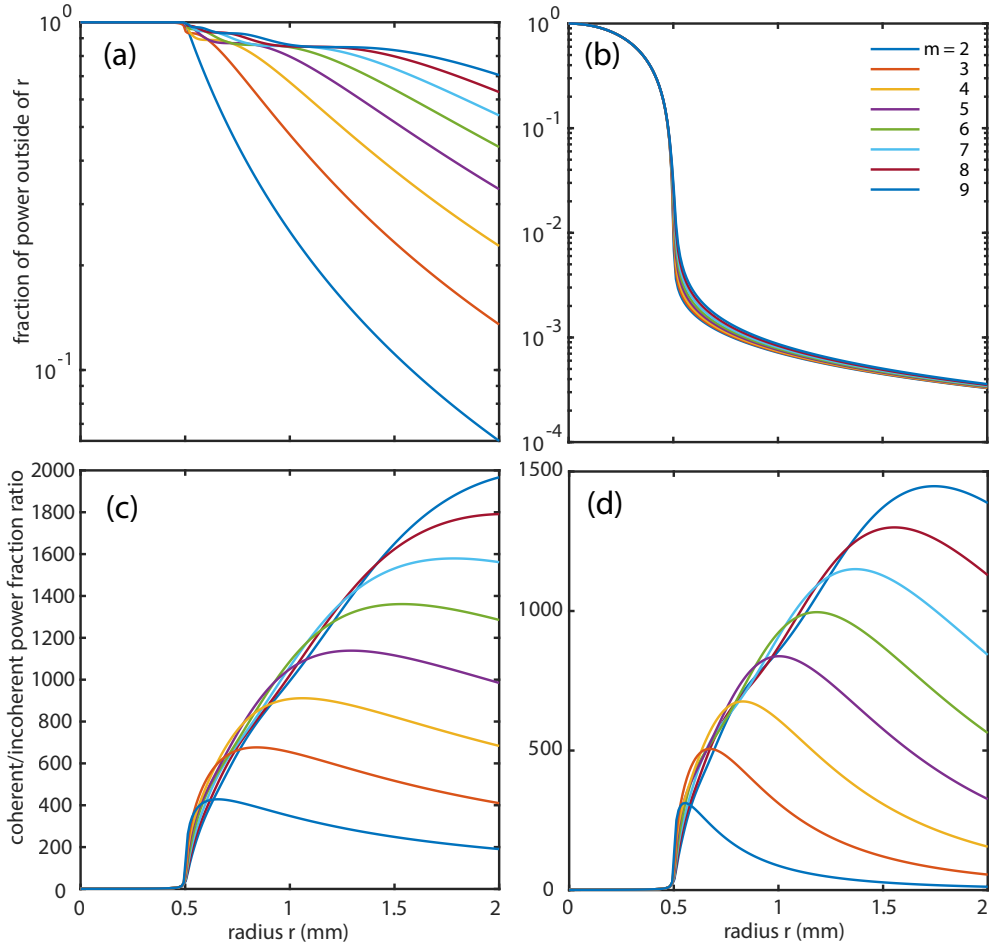

Fig. 4. Escaping power fractions and coherent-incoherent (CI) power ratios using the setup described in Fig. 1(d). (a) The fraction of on-axis coherent power that escapes around a beam block of radius r for using vortex plates of various listed topological charge. (b) The fraction of incoherent power that escapes around a beam block of radius r. (c) The CI ratio defined by the curves in (a) divided by those in (b) of corresponding color. (d) The coherent power weighted CI ratio defined by the square of the curves in (a) divided by the curves in (b) of corresponding color. The incoherent source is a distant spherical cap that subtends 8 degrees as measured from the entrance pupil.

spreading due to lenses, while h, as described by Eq. 11, was used in generating the red curves. A pinhole radius near zero maximizes Q_A, but a radius near zero would pass no power and would be useless in a real experiment, which again indicates that Q_B is the more useful ratio. A pinhole radius of 52.8 um maximizes Q_B on the blue curve, which in general depends on the radius of the entrance pupil, the wavelength of the light, and the focal length of L_1. Reaching a peak value of $Q_B = 16250$ on both the blue and red curves, the pinhole spatial filter Q_B peak is about 11 times higher than that of the $m = 9$ vortex peak listed in Table 1. Using Q_B as a measure for the efficacy of a system in filtering out incoherent light, this result indicates that a pinhole spatial filter is around 11 times more effective than an $m = 9$ vortex phase plate, which itself has the highest peak Q_B in Fig. 4(d).

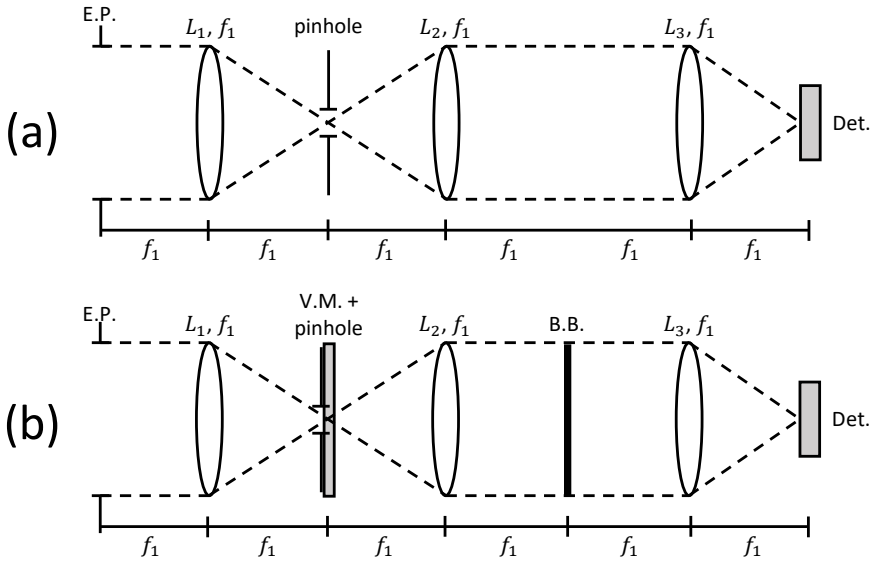

Fig. 5. Alternatives to the optical configuration of Fig. 1(d). (a) A pinhole spatial filter. (b) A vortex-mask and pinhole combination. V.M. indicates a vortex mask, E.P. indicates an entrance pupil, B.B. indicates a beam block, and Det. indicates a detector.

6.3. Vortex and pinhole combined

If both the pinhole spatial filter and the vortex mask can be used to separate coherent light from incoherent light, and if they use different mechanisms to do so, then it may be possible to combine the two to achieve better results than either can achieve individually. To explore this idea, we simulate the optical system shown in Fig. 5(b). This system is identical to that of Fig. 1(d) except a pinhole has been added to the plane of the vortex mask. We consider four different cases by combining vortex mask charges 2 and 8 with pinhole radii 52.8 and 75 um, and we use a Dirac delta impulse response (without lens diffraction) function for s implicity. Here, Q_A and Q_B are defined as in the vortex-only case.

Plots of the CI escaping power ratio functions are given in Figs. 6(c) and 6(d). The horizontal dashed lines indicate the ratio without a beam block, with only the pinhole acting as a filter, and correspond to the points on the blue curve in Fig. 6(b) at radii 52.8 and 75 um. In every case, the addition of a vortex mask to a pinhole spatial filter increases the CI ratio under a range of beam block radii. A table of the maxima and percentage increase versus the pinhole alone are given in Table 2. In the case of the optimum pinhole radius (52.8 um), the benefit of adding the vortex mask is small for both $m = 2$ and $m = 8$, adding only about 2% to Q_B. For the non-optimum radius (75 um), the benefit of adding the vortex mask is more substantial and adds almost 10% in the $m = 8$ case, although it stops another 15% short of restoring the Q_B ratio of the optimum pinhole.

7. Conclusion

Here, we have considered a modified optical vortex coronagraph system for theoretical use in a transmissometer mode. For an on-axis coherent source combined with an 8-degree, on-axis incoherent source, we found, using Fourier optical theory, that the system is capable of rejecting scattered, spatially incoherent light relative to coherent light at ratios greater than 1000:1 when

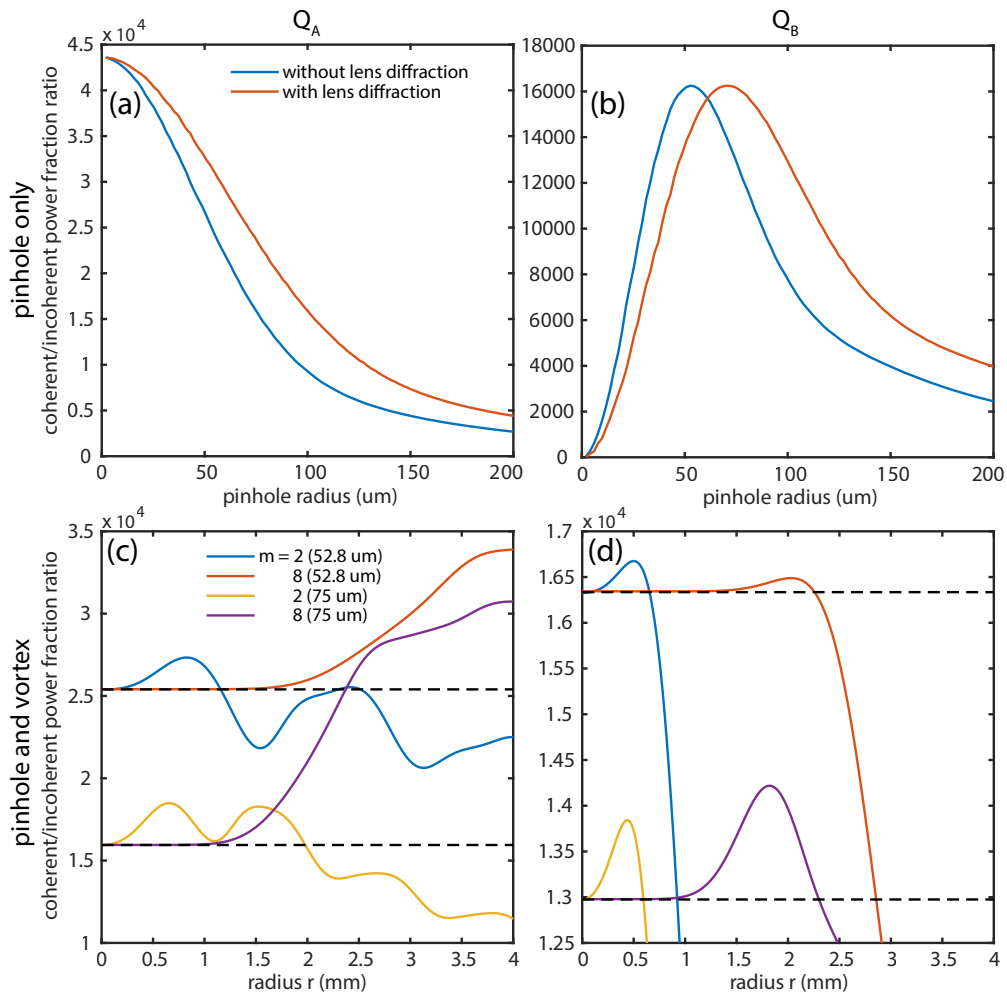

Fig. 6. Coherent-incoherent (CI) power ratios using the setups described in Fig. 5. (a) The CI ratio and (b) the coherent power weighted CI ratio versus pinhole radius under the pinhole-only setup given in Fig. 5(a). The blue curves indicate simulations that neglect diffraction by the lenses and red curves include lens diffraction. (c) The CI ratio and (d) the coherent power weighted CI ratio versus beam-block radius r under the vortex mask and pinhole combination setup given in Fig. 5(b). The curves represent changing the vortex charge number m and pinhole radius (in parentheses).

using vortex charges between 6 and 9. We showed that this ratio tends linearly upwards with charge number and expect it to increase further with higher charge numbers. We compared the vortex system to that employing a pinhole alone and found that the pinhole-only system outperforms a charge = 9 vortex system by an order of magnitude. However, by combining the optical vortex phase element in the image plane of the coronagraph with a pinhole, we showed that the combined system can achieve a rejection ratio 1-10% greater than that of the pinhole alone, depending on the pinhole size and vortex charge. Due to the extreme separation of light from coherent versus incoherent sources, we expect transmissometers that employ an optical vortex coronagraph, set up in a transmissometer mode with both a vortex element and pinhole (see Fig. 5b), to outperform those that employ either a vortex element or a pinhole alone.

vortex charge m	arg max Q_A (R_0)	max Q_A	arg max Q_B (R_0)	max Q_B
2	1.3	420	1.1	310
3	1.7	680	1.3	500
4	2.1	910	1.7	680
5	2.6	1100	2.0	840
6	3.1	1400	2.4	1000
7	3.6	1600	2.7	1200
8	4.1	1800	3.1	1300
9	4.6	2000	3.5	1400

Table 1. Beam block optimal radius and the integrated coherent-to-incoherent ratio as a function of vortex charge number. arg max is in units of multiples of the entrance pupil radius R_0.

vortex charge m	pinhole radius (um)	arg max Q_B (R_0)	max Q_B	gain vs. pinhole (%)
2	52.8	1.01	16675	2.6
8	52.8	4.06	16490	1.4
2	75	0.88	13840	6.7
8	75	3.66	14220	9.6

Table 2. Beam block optimal radius, coherent power weighted CI ratio, and gain in CI ratio versus a pinhole alone, as a function of vortex charge number m and pinhole radius. arg max is in units of multiples of the entrance pupil radius R_0.

8. Funding

Funding provided by Naval Research Laboratory 6.1 Base Program.

9. Acknowledgments

Authors thank the Eric Johnson group at Clemson University for fabrication of the phase masks that motivated the simulations described in this paper.

10. Disclosures

The authors declare no conflicts of interest.

References

1. D. Palacios, D. Rozas, and G. A. Swartzlander Jr, "Observed scattering into a dark optical vortex core," Phys. review letters **88**, 103902 (2002).
2. L. Wan, G. J. Ruane, and G. A. Swartzlander, "Low-angle optical vortex coronagraphic scatterometer," Opt. letters **41**, 4915–4918 (2016).

3. G. A. Swartzlander Jr, "The optical vortex coronagraph," J. Opt. A: Pure Appl. Opt. **11**, 094022 (2009).
4. G. Foo, D. M. Palacios, and G. A. Swartzlander, "Optical vortex coronagraph," Opt. Lett. **30**, 3308–3310 (2005).
5. B. Cochenour, L. Rodgers, A. Laux, L. Mullen, K. Morgan, J. K. Miller, and E. G. Johnson, "The detection of objects in a turbid underwater medium using orbital angular momentum (OAM)," in *Ocean Sensing and Monitoring IX,* vol. 10186 W. W. Hou and R. A. Arnone, eds., International Society for Optics and Photonics (SPIE, 2017), p. 1018603.
6. B. Cochenour, A. Alley, A. E. Laux, and L. Mullen, "Optical vortex transmissometer," US Patent number US-11480522-B2. https://image-ppubs.uspto.gov/dirsearch-public/print/downloadPdf/11480522 (2022).
7. A. Jantzi, L. Rumbaugh, and W. Jemison, "Spatial coherence filtering for scatter rejection in underwater laser systems," in *Ocean Sensing and Monitoring XI,* vol. 11014 (SPIE, 2019), pp. 20–29.
8. A. Jantzi, W. Jemison, D. Illig, and L. Mullen, "Axicons for improved lidar performance," in *Ocean Sensing and Monitoring XII,* vol. 11420 (SPIE, 2020), pp. 67–79.
9. A. Jantzi, W. Jemison, A. Laux, L. Mullen, and B. Cochenour, "Enhanced underwater ranging using an optical vortex," Opt. express **26**, 2668–2674 (2018).
10. E. Wolf, *Introduction to the Theory of Coherence and Polarization of Light* (Cambridge university press, 2007).
11. J. Goodman, *Introduction to Fourier Optics* (Roberts & Company, 2005), 3rd ed.